

Poincaré-sphere symmetries in four-wave mixing with orbital angular momentumM. R. L. da Motta ^{1,*}, G. B. Alves ^{2,†}, A. Z. Khoury ^{2,‡} and S. S. Vianna ^{1,§}¹*Departamento de Física, Universidade Federal de Pernambuco, 50670-901 Recife, Pernambuco, Brazil*²*Instituto de Física, Universidade Federal Fluminense, 24210-346 Niterói, Rio de Janeiro, Brazil*

(Received 23 August 2023; revised 17 November 2023; accepted 19 December 2023; published 11 January 2024)

We explore a degenerate four-wave mixing process induced by transversely structured light beams in a rubidium vapor cell. In particular, we consider the nonlinear interaction driven by optical modes contained in the orbital angular momentum Poincaré sphere, which can be parametrized in terms of a polar and an azimuthal angle. In this context we investigate the transfer of spatial structure to two distinct four-wave mixing (FWM) signals, possessing different propagation directions in space. We show that under usual assumptions, the output fields can also be described by modes belonging to Poincaré spheres, and that the angles describing the input and output modes are related according to well-defined rules. Our experimental results show good agreement with the calculations, which predict intricate field structures and a transition of the FWM transverse profile between the near- and far-field regions.

DOI: [10.1103/PhysRevA.109.013506](https://doi.org/10.1103/PhysRevA.109.013506)**I. INTRODUCTION**

In recent years, the spatial structure of light has seen a significant increase in research interest, both in fundamental studies and in applications and technological developments [1]. The understanding of effects attributed to the transverse structure of light in optical phenomena and the ability to control the spatial degrees of freedom of the light field have allowed numerous advances in the optical sciences [2]. We may highlight fundamental properties of electromagnetic radiation [3,4], quantum optics [5,6], manipulation of matter [7,8], holography [9], information multiplexing [10–12], quantum communication [13,14], metrology [15], and nonlinear light-matter interactions [16–21].

The starting point of these advances can be traced back to 1992, when the seminal work of Allen *et al.* [22] established the connection between the orbital angular momentum (OAM) of a light beam and its spatial distribution. This breakthrough originated the field of light OAM, which over the past three decades has grown immensely and has transformed in such a way as to be recognized today as the more general field of structured light [1]. Shortly after these advancements, the investigation of the role played by OAM in nonlinear optical processes started in second-order harmonic generation (SHG) [23–25]. Today, SHG and other second-order optical phenomena offer a highly versatile platform to study the transverse degrees of freedom of light.

Four-wave mixing, a third-order nonlinear optical process, has also been extensively employed in the context of structured light [21,26–32]. The parametric gain in free space four-wave mixing is considerably higher than

in three-wave processes. Moreover, four-wave mixing has become an important method for generating quantum-correlated beams [26]. These quantum correlations have been used to produce OAM-multiplexed continuous-variable entanglement, allowing deterministic all-optical quantum teleportation and quantum dense coding [33–35]. The achievements in quantum-correlated OAM beams produced by four-wave mixing includes the recent demonstration of tripartite entanglement [36].

Within the seemingly endless sea of structured light [2], one finds the optical modes belonging to the so-called OAM Poincaré sphere (PS) [37], named in analogy with the polarization Poincaré sphere. They are given by combinations of Laguerre-Gaussian (LG) modes with topological charges of equal magnitude and opposite handedness, and can be parametrized in terms of polar and azimuthal angles on the sphere. OAM PS modes have been widely employed in three-wave mixing in nonlinear crystals [16–18,38,39]. The interplay between spin and orbital angular momentum in second-order harmonic generation has also been demonstrated [19,20,40]. The OAM mixing in second-order nonlinear media has been shown to be constrained by several selection rules, which involve OAM conservation [25,41], radial-angular coupling [18,20,42,43], and Poincaré-sphere symmetry [38,39,44]. The PS symmetry has also been investigated in the quantum domain of optical parametric oscillation with OAM beams, where continuous-variable hyperentanglement has been predicted [45] and experimentally demonstrated [46]. The connection between this symmetry and phase conjugation in the parametric process [47] has been discussed in Ref. [48].

In this work we explore the geometrical representation in the Poincaré sphere to experimentally investigate the nonlinear wave mixing induced by OAM PS beams in a heated sample of rubidium atoms, and the underlying rules that dictate the transfer of optical spatial structure. In particular, we consider a degenerate forward four-wave mixing (FWM)

*mateus.motta@ufpe.br

†gbie@id.uff.br

‡azkhoury@id.uff.br

§sandra.vianna@ufpe.br

process in a configuration where two distinct signals are generated [49,50], and extend previous studies by analyzing the nonlinear response when the input beams can be described as a combination of LG modes, and going beyond the OAM conservation selection rules. Moreover, we theoretically describe both generated beams and show that, under the usual set of assumptions, they can also be represented as optical modes contained in Poincaré spheres. An interesting point is that, as we demonstrate, the PS components of both four-wave mixing outputs satisfy selection rules similar to those verified in three-wave mixing processes, namely, (i) a specular reflection symmetry in the Poincaré sphere, which is observed in the down-conversion process [38,39,44], and (ii) the generation of a radial mode spectrum which has been demonstrated in second-order harmonic generation [18,42]. These results indicate that most applications that make use of the OAM degree of freedom of a light beam can be extended to a higher-order nonlinear process. Furthermore, our two-channel FWM configuration allows us to simultaneously detect two nonlinear signals, each exhibiting a characteristic: the reflection symmetry in the Poincaré sphere and the appearance of a radial mode spectrum in the spatial structure, both already explored independently in three-wave mixing processes. The predicted FWM intensity, as well as the consequences of the symmetry properties, are in good agreement with our experimental results.

II. THEORY

To describe the nonlinear light-matter interaction associated with the generation of two degenerate four-wave mixing outputs, we consider two driving laser beams named \mathbf{E}_a and \mathbf{E}_b , with the same frequency $\omega_a = \omega_b$, and wave vectors \mathbf{k}_a and \mathbf{k}_b , separated by a small angle. The two beams propagate inside the third-order nonlinear medium of length L , from $z = -L/2$ to $z = L/2$, intersecting at the center, $z = 0$, the position at which their waists are minimum. Two four-wave mixing signals can be generated as a result of the interaction of the input beams with the atomic medium. These fields are \mathbf{E}_1 , associated with the absorption of two photons from \mathbf{E}_a and the stimulated emission of one photon from \mathbf{E}_b , and \mathbf{E}_2 , associated with the absorption of two photons from \mathbf{E}_b and the stimulated emission of one photon from \mathbf{E}_a . Due to the conservation of energy and linear momentum, the FWM fields \mathbf{E}_1 and \mathbf{E}_2 are generated with frequencies $\omega_1 = \omega_2 = \omega_{a,b}$, and in the directions given by $(2\mathbf{k}_a - \mathbf{k}_b)$ and $(2\mathbf{k}_b - \mathbf{k}_a)$, respectively. Figure 1(a) shows the spatial orientation of the incident and generated light beams. For linearly polarized incident beams with orthogonal polarizations, the interaction can be seen as taking place in a three-level atomic system, constituted of two degenerate ground states $|1\rangle$, $|3\rangle$, and an excited state $|2\rangle$. Each generated signal can be seen as a contribution from two pathways starting from different ground states, as illustrated in Fig. 1(b) for the field \mathbf{E}_1 .

The electric fields of the light beams participating in the FWM processes are written as

$$\mathbf{E}_i(\mathbf{r}, t) = \frac{1}{2} \boldsymbol{\epsilon}_i \mathcal{E}_i(\mathbf{r}) e^{-i(\mathbf{k}_i \cdot \mathbf{r} - \omega_i t)} + \text{c.c.}, \quad (1)$$

$i \in \{a, b, 1, 2\}$, where $\boldsymbol{\epsilon}_i$ is the polarization direction, \mathcal{E}_i is the slowly varying field amplitude, \mathbf{k}_i is the wave vector, and

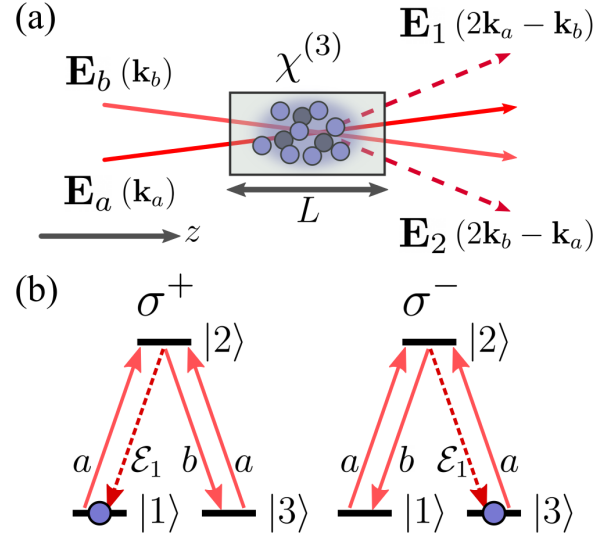


FIG. 1. (a) Spatial orientation of incident and generated signals near the interaction region. (b) Two pathways associated with the generation of the σ^\pm components of the FWM signal \mathbf{E}_1 in a three-level atomic system.

$\omega_i = c|\mathbf{k}_i|$ is the frequency. The wave equations describing evolution of the slowly varying FWM field envelopes \mathcal{E}_1 and \mathcal{E}_2 , as a result of the two independent FWM processes in directions $(2\mathbf{k}_a - \mathbf{k}_b)$ and $(2\mathbf{k}_b - \mathbf{k}_a)$, are [49]

$$\left(\frac{i}{2k_1} \nabla_\perp^2 + \frac{\partial}{\partial z} \right) \mathcal{E}_1 = \kappa_1 \mathcal{E}_a^2 \mathcal{E}_b^* e^{-i\Delta k_1 z}, \quad (2)$$

$$\left(\frac{i}{2k_2} \nabla_\perp^2 + \frac{\partial}{\partial z} \right) \mathcal{E}_2 = \kappa_2 \mathcal{E}_b^2 \mathcal{E}_a^* e^{-i\Delta k_2 z}, \quad (3)$$

where the couplings κ_1 and κ_2 are proportional to the nonlinear susceptibilities associated with the two nonlinear processes, χ_1 and χ_2 , and Δk_1 and Δk_2 are the phase mismatches. Owing to the orthogonality and completeness of paraxial modes, we can write the solutions to Eqs. (2) and (3) as general superpositions of the form

$$\mathcal{E}_1(\mathbf{r}) = \sum_{\ell,p} \alpha_{\ell,p} u_{\ell,p}(\mathbf{r}), \quad (4)$$

$$\mathcal{E}_2(\mathbf{r}) = \sum_{\ell,p} \beta_{\ell,p} u_{\ell,p}(\mathbf{r}), \quad (5)$$

where $u_{\ell,p}$ is the LG mode, denoted as

$$u_{\ell,p}(\mathbf{r}) = \frac{C_{\ell,p}}{w(z)} \left(\frac{\sqrt{2}r}{w(z)} \right)^{|\ell|} L_p^{|\ell|} \left(\frac{2r^2}{w^2(z)} \right) e^{-\frac{r^2}{w^2(z)}} \times e^{i\ell\gamma} \exp \left(-i \frac{kr^2}{2R(z)} + i\Psi_G(z) \right), \quad (6)$$

where we write the position vector in cylindrical coordinates as $\mathbf{r} = (r, \gamma, z)$, $C_{\ell,p} = \sqrt{2p!/\pi(p+|\ell|)!}$ is a normalization constant, $L_p^{|\ell|}(\cdot)$ is the associated Laguerre polynomial, $w(z) = w_0 \sqrt{1 + (z/z_R)^2}$ is the beam width, $R(z) = z[1 + (z_R/z)^2]$ is the curvature radius, and $\Psi_G(z) = (N_{\ell,p} + 1) \tan^{-1}(z/z_R)$ is the Gouy phase shift, with the total mode order defined as $N_{\ell,p} = 2p + |\ell|$. It is important to note

that families of modes $\{u_{\ell,p}\}$ with different spot sizes w_0 form different bases.

We consider that the incident fields can be written as $\mathcal{E}_a(\mathbf{r}) = \mathcal{E}_a^0 u_a(\mathbf{r})$ and $\mathcal{E}_b(\mathbf{r}) = \mathcal{E}_b^0 u_b(\mathbf{r})$, where $\mathcal{E}_{a,b}^0$ gives the total power content of each field, $P_{a,b} = \frac{1}{2} c \varepsilon_0 |\mathcal{E}_{a,b}^0|^2$, and $u_{a,b}(\mathbf{r})$ carries their spatial structure. Taking into account that the paraxial basis modes $\{u_{\ell,p}\}$ carry the information from the transverse structure of the generated fields $\mathcal{E}_{1,2}$, the problem becomes that of finding the expansion coefficients $\alpha_{\ell,p}$ and $\beta_{\ell,p}$. They are called the full spatial overlap integrals, and can be expressed as [51]

$$\alpha_{\ell,p} = \kappa_1 \mathcal{E}_1^0 \int_{-L/2}^{L/2} \mathcal{A}_{\ell,p}(z) e^{-i\Delta k_1 z} dz, \quad (7)$$

$$\beta_{\ell,p} = \kappa_2 \mathcal{E}_2^0 \int_{-L/2}^{L/2} \mathcal{B}_{\ell,p}(z) e^{-i\Delta k_2 z} dz, \quad (8)$$

where $\mathcal{E}_1^0 = (\mathcal{E}_a^0)^2 (\mathcal{E}_b^0)^*$, $\mathcal{E}_2^0 = (\mathcal{E}_b^0)^2 (\mathcal{E}_a^0)^*$, and

$$\mathcal{A}_{\ell,p}(z) = \iint u_a^* u_b^* u_{\ell,p}^* d^2 \mathbf{r}_\perp, \quad (9)$$

$$\mathcal{B}_{\ell,p}(z) = \iint u_b^* u_a^* u_{\ell,p}^* d^2 \mathbf{r}_\perp, \quad (10)$$

are the transverse overlap integrals of the product of incident beams on the mode basis with waist w_0 . In the thin-medium regime, characterized by $L/z_R \ll 1$, only the transverse overlap integrals evaluated at $z = 0$ are relevant for calculations [49]. We may therefore write

$$\alpha_{\ell,p} \simeq \kappa_1 \mathcal{E}_1^0 T_1(L) \mathcal{A}_{\ell,p}(0), \quad (11)$$

$$\beta_{\ell,p} \simeq \kappa_2 \mathcal{E}_2^0 T_2(L) \mathcal{B}_{\ell,p}(0), \quad (12)$$

where $T_j(L) = \int_{-L/2}^{L/2} e^{-i\Delta k_j z} dz = L \text{sinc}(\Delta k_j L/2)$, $j = 1, 2$, can be seen as efficiency measures of the wave-mixing processes. Note that the factors $\kappa_j \mathcal{E}_j^0 T_j(L)$ are common for all (ℓ, p) , and therefore do not affect the mode superpositions of the generated fields. We do not carry these factors further. Now we can explore scenarios where the incident beams \mathcal{E}_a and \mathcal{E}_b carry different structures.

We will focus on the situation where field u_b is given by a pure Gaussian mode, $u_{0,0}$, and u_a is given by the composition of LG modes contained in the OAM Poincaré sphere $\mathcal{O}(l, 0)$ (see Fig. 2):

$$\psi_{l,0}(\theta, \phi) = \cos \frac{\theta}{2} u_{l,0} + e^{i\phi} \sin \frac{\theta}{2} u_{-l,0}. \quad (13)$$

The Poincaré sphere construction applies to two-dimensional complex vector spaces, but there is not a special restriction to the modes used in either input field \mathcal{E}_a or \mathcal{E}_b . This is because even when several modes participate in either three- or four-wave parametric interactions, the interacting modes can be grouped in pairs with opposite OAM, plus the zero-OAM modes, when they are present. Each pair of opposite-OAM modes builds an independent Poincaré sphere. The geometrical representation of the nonlinear interaction that we will establish, and the associated symmetries, apply to each sphere independently [39]. Of course, there is no room for these symmetries in the zero-OAM manifold. Upon substitution in

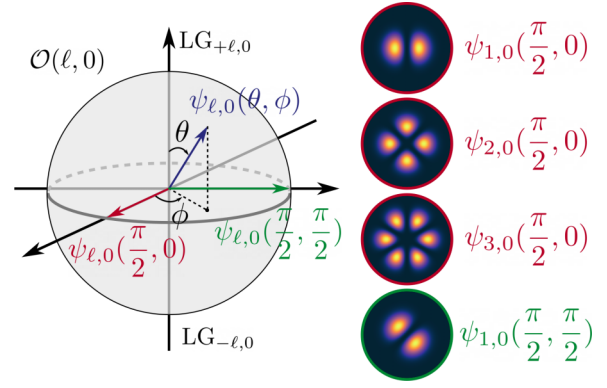


FIG. 2. Representation of a spatial mode as a vector parametrized by the polar θ and azimuthal ϕ angles on the OAM Poincaré sphere $\mathcal{O}(l, 0)$, and intensity profile of different modes on the sphere equator, $\theta = \pi/2$.

Eqs. (9) and (10), we can write the transverse overlap integrals at $z = 0$ as

$$\mathcal{A}_{\ell,p}(0) = \cos^2 \frac{\theta}{2} \Lambda_{000p}^{l\ell} + e^{2i\phi} \sin^2 \frac{\theta}{2} \Lambda_{000p}^{-l,-l\ell} + e^{i\phi} \sin \theta \Lambda_{000p}^{l,-l\ell}, \quad (14)$$

$$\mathcal{B}_{\ell,p}(0) = \cos \frac{\theta}{2} \Lambda_{000p}^{00\ell} + e^{-i\phi} \sin \frac{\theta}{2} \Lambda_{000p}^{00,-l\ell}, \quad (15)$$

where

$$\Lambda_{qq'np}^{ll'm\ell} = \iint u_{l,q} u_{l',q'} u_{m,n}^* u_{\ell,p}^* |_{z=0} d^2 \mathbf{r}_\perp \quad (16)$$

is the transverse overlap integral of four LG modes with the same waist w_0 . The conservation of OAM naturally emerges from the azimuthal integral

$$\int_0^{2\pi} e^{i(l+l'-m-\ell)\gamma} d\gamma = 2\pi \delta_{\ell,l+l'-m}, \quad (17)$$

restricting the possible values for the topological charges contained in the superpositions for \mathcal{E}_1 and \mathcal{E}_2 . For signal \mathcal{E}_1 , we will have modes with $\ell = \pm 2l$ [first and second terms of Eq. (14)], yielding the contribution from a PS of order $N = 2l$, and also from $\ell = 0$, while for signal \mathcal{E}_2 , we only have the $\ell = \pm l$ components [Eq. (15)], associated with a PS of the same order $N = l$ as the input. In principle, there is no such restriction on the radial orders, and an infinite number of p modes can contribute to the superpositions of the fields \mathcal{E}_1 and \mathcal{E}_2 . It is important to note that for the third-order process studied here, the possible values for the topological charges imposed by the azimuthal integral, Eq. (17), are the same as those found in second-order processes, namely, in SHG, where the process is driven by a structured pump, from which two photons are absorbed to generate the up-converted field, as in the case of signal \mathcal{E}_1 , and in the down-conversion process, where the medium is excited by a Gaussian pump, and the down-converted fields are the ones carrying the spatial structure, a situation analogous to that of signal \mathcal{E}_2 .

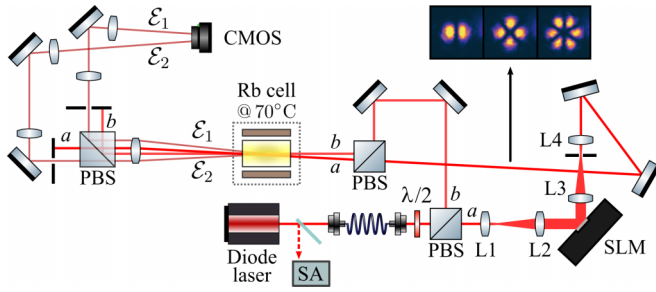


FIG. 4. Simplified scheme of the experimental setup for the detection of FWM beam profiles. The pairs of lenses L1-L2 and L3-L4 form telescopes to increase and decrease the diameter of the beam modulated by the SLM. The spatial filters, formed by pairs of lenses and a pinhole at the focal plane, were positioned on the path of both FWM signals.

inside a 5-cm-long cell. We detect the two four-wave mixing signals \mathbf{E}_1 and \mathbf{E}_2 generated in the $(2\mathbf{k}_a - \mathbf{k}_b)$ and $(2\mathbf{k}_b - \mathbf{k}_a)$ directions, respectively. Since \mathbf{E}_a and \mathbf{E}_b possess orthogonal polarizations, the generated fields \mathbf{E}_1 and \mathbf{E}_2 are also orthogonally polarized with respect to each other. Moreover, \mathbf{E}_1 (\mathbf{E}_2) is orthogonally polarized with respect to \mathbf{E}_a (\mathbf{E}_b). This results in an arrangement at the output where the four signals possess alternating polarizations.

We arrange the setup in such a way that the minimum waists of both incident beams are located inside the vapor cell, where they intercept. The rubidium cell, containing both ^{87}Rb and ^{85}Rb in natural abundances, is heated to about 70°C to increase atomic density. For all measurements, we considered the $|5^2S_{1/2}, F_g = 3\rangle \rightarrow |5^2P_{3/2}\rangle$ transition of ^{85}Rb . Since the nonlinear output is much weaker than the transmitted beams, scattered light from the input beams was a big problem, especially because we work in a degenerate configuration, and we circumvented this issue by using spatial filters on the paths of both FWM beams. The waists of the incident beams at

the location of the cell were $w_0 \approx 0.5$ mm. This gives the Rayleigh range value of $z_R = \pi w_0^2/\lambda \approx 1$ m. For a cell of length $L = 5$ cm, we assume that the thin-medium regime ($L/z_R \ll 1$) is always satisfied.

IV. RESULTS AND DISCUSSION

First, we performed experiments by setting field \mathcal{E}_a as a mode on the equator ($\theta = \pi/2$) of the PS $\mathcal{O}(\ell, 0)$, $\psi_{\ell,0}^{(a)}(\pi/2, 0)$ [see Fig. 5(a)], and field \mathcal{E}_b as a pure Gaussian beam. Figures 5(b) and 5(c) show the calculated and measured far-field intensity profiles of the generated signals, \mathcal{E}_2 and \mathcal{E}_1 , respectively. We see that for signal \mathcal{E}_1 [Fig. 5(c)] we obtain more intricate figures, while the structure of signal \mathcal{E}_2 [Fig. 5(b)] seems to be dominated by that of the pump in each case. This is due to the fact that signal \mathcal{E}_1 has two contributions from the structured pump, and the nonlinear polarization associated with its generation is proportional to $(\psi_{\ell,0}^{(a)})^2$. On the other hand, for \mathcal{E}_2 , which has only one contribution from \mathcal{E}_a , the macroscopic polarization is proportional to $(\psi_{\ell,0}^{(a)})^*$.

The central spots present in signal \mathcal{E}_1 are due to the contribution from the $\ell = 0$ modes arising from the crossed term in the product $(\psi_{\ell,0}^{(a)})^2$. They only develop in the far field because of the difference in Gouy phases with respect to the 2ℓ modes. This becomes evident when one looks at the near-field intensity distributions of the FWM signal \mathcal{E}_1 for $\ell = 1, 2$, shown in Fig. 5(d). This type of transition of the transverse structure has been verified in other situations [18,29,53]. This behavior is not verified for signal \mathcal{E}_2 , since it only contains the PS mode with total order $N = |\ell|$, and therefore its shape is stable under propagation. Finally, it is worth commenting on the distortions seen in the experimental images. This is due to the degenerate configuration we are working with, which makes it difficult to completely filter the scattered light superimposed to the spatial profiles of the generated signals.

We also made the pump field u_a occupy different positions on the PS. First we consider u_a following a path starting on

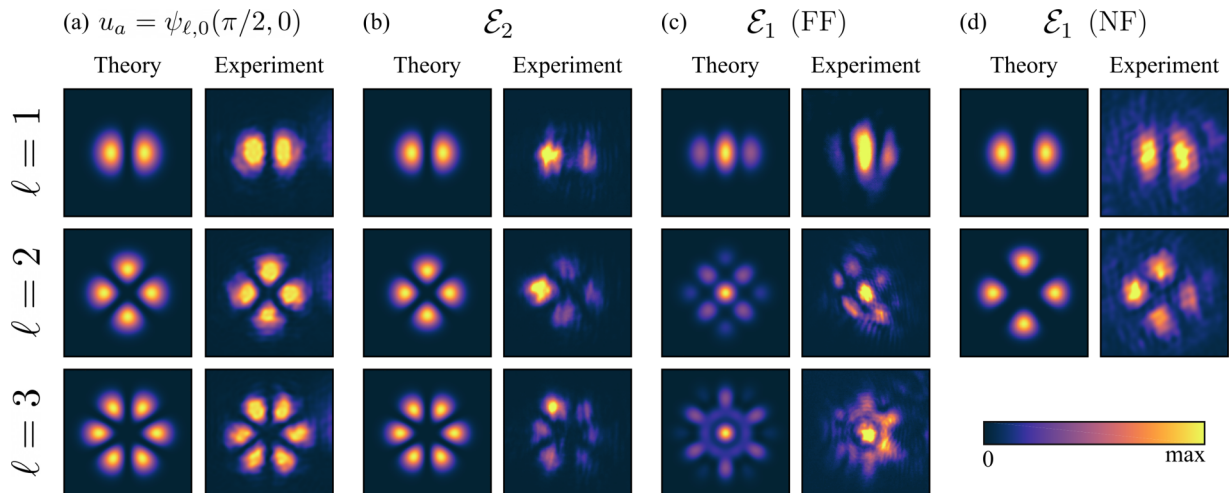


FIG. 5. (a) Calculated intensity profiles of modes $\psi_{\ell,0}(\pi/2, 0)$, for $\ell = 1, 2, 3$, alongside the corresponding beams prepared in the experiment near the interaction region. Calculated and detected far-field intensity profiles of the FWM signals (b) \mathcal{E}_2 and (c) \mathcal{E}_1 , resulting from the mixing of u_a given by the modes shown in (a) and u_b given by a Gaussian mode. (d) Calculated and detected near-field intensity profiles of the FWM signal \mathcal{E}_1 for the cases $\ell = 1, 2$.

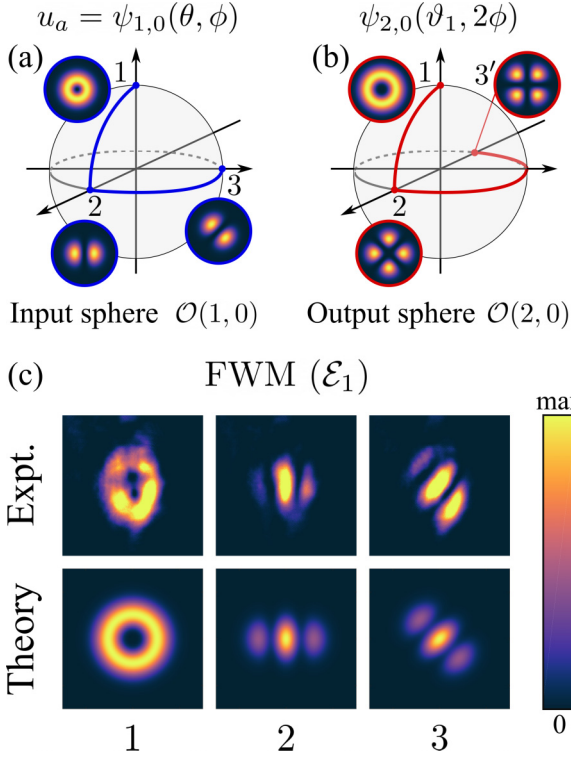


FIG. 6. (a) Incident field modes along a path described by points 1, 2, and 3 on the first-order sphere $\mathcal{O}(1, 0)$. (b) Corresponding modes on the output sphere $\mathcal{O}(2, 0)$ for the FWM signal \mathcal{E}_1 , when $u_b = u_{0,0}$. Insets show the intensity profiles of the sphere modes on the indicated positions. (c) Measured (top) and calculated (bottom) FWM intensity profiles for signal \mathcal{E}_1 when the mode vector of field u_a is located on the points 1, 2, and 3 along the path shown in (a).

the positive pole, $(\theta, \phi) = (0, 0)$, going to $(\pi/2, 0)$ on the equator, and then to $(\pi/2, \pi/2)$. We call these points 1, 2, and 3, respectively [see Fig. 6(a)]. The incident modes in these positions are $\psi_{1,0}(0, 0) = u_{1,0}$, $\psi_{1,0}(\pi/2, 0) = (u_{1,0} + u_{-1,0})/\sqrt{2}$, and $\psi_{1,0}(\pi/2, \pi/2) = (u_{1,0} + iu_{-1,0})/\sqrt{2}$. Figure 6(b) shows the corresponding path followed by the PS component of the FWM field \mathcal{E}_1 on the output sphere $\mathcal{O}(2, 0)$. In Fig. 6(c), we show the experimental and theoretical far-field intensity profiles of signal \mathcal{E}_1 in this case. For point 1, where u_a is a pure $u_{1,0}$ mode, the field \mathcal{E}_1 emerges as a pure $u_{2,0}$ mode, and we are essentially performing OAM addition [50]. As we leave the pole, we can employ the PS geometric representation to interpret the behavior of the FWM output field structure. We see that the actual FWM intensity profiles differ from those expected solely from a PS mode $\psi_{2,0}$ on points 2 and 3, corresponding to the first term on the right-hand side (r.h.s.) of Eq. (22). This is due to the contribution from the radial modes in the superposition \mathcal{E}_1 , which becomes maximum when $\theta = \pi/2$, as seen from the second term on the r.h.s. of Eq. (22).

What is remarkable from these results is that the variation of the azimuthal angle ϕ on the input sphere results in a rigid rotation of the FWM intensity profile that is equal to the rotation of the intensity profile of u_a . This is not obvious since, as already mentioned, (i) the azimuthal angle on the output sphere is doubled, $\varphi_1 = 2\phi$, and (ii) there are radial modes contributing to the FWM field mode structure. In fact,

this net effect is precisely a result of the combination of these two aspects. To explain this, we first look at the rotation of the intensity profile of the input PS mode $\psi_{l,0}(\theta, \phi)$, $\mathcal{I}_l(\mathbf{r}_\perp; \theta, \phi) = |\psi_{l,0}(\theta, \phi)|^2$, which can be understood when we write

$$\mathcal{I}_l(r, \gamma; \theta, \phi) = |u_{l,0}|^2 \left\{ 1 + \sin \theta \cos 2l \left(\gamma - \frac{\phi}{2l} \right) \right\}. \quad (26)$$

We see that the PS azimuthal angle ϕ shifts the origin of the transverse azimuthal coordinate γ as

$$\mathcal{I}_l(r, \gamma; \theta, \phi) = \mathcal{I}_l(r, \gamma - \phi/2l; \theta, 0), \quad (27)$$

thus rotating the intensity profile by $+\phi/2l$. This can be verified by looking at Figs. 6(a) and 6(b), where we see the intensity profiles of the modes on the spheres $\mathcal{O}(1, 0)$ and $\mathcal{O}(2, 0)$ rotate by 45° when the azimuthal angles vary by 90° and 180° , respectively. The intensity profile of the FWM field \mathcal{E}_1 , $I_1 = |\mathcal{E}_1|^2$, can be found as

$$\begin{aligned} I_1(r, \gamma; \theta, \phi) &= \sin^2 \theta |U_l|^2 + |\tilde{a}_0|^2 |\tilde{u}_{2l,0}|^2 \\ &\times \left\{ 1 + \sin \vartheta_1 \cos \left[4l \left(\gamma - \frac{\phi}{2l} \right) \right] \right\} \\ &+ 2\sqrt{2}\tilde{a}_0\tilde{V}_0^{2l} U_l \sin \theta \sin \left(\frac{\vartheta_1}{2} + \frac{\pi}{4} \right) \\ &\times \cos \left[2l \left(\gamma - \frac{\phi}{2l} \right) \right], \end{aligned} \quad (28)$$

where the LG radial amplitude $\tilde{V}_p^{|\ell|}(r)$ is defined via $\tilde{u}_{\ell,p}(r, \gamma) = \tilde{V}_p^{|\ell|}(r)e^{i\ell\gamma}$, and $U_l = \sum_{p=0}^{|l|} \tilde{c}_p \tilde{u}_{0,p}$ is the term from Eq. (22) containing the superposition of radial modes. Thus, we see that, just like in Eq. (26), I_1 presents a shift of the transverse azimuthal coordinate by the amount $\phi/2l$, equal to that of the input PS mode $\psi_{l,0}$:

$$I_1(r, \gamma; \theta, \phi) = I_1(r, \gamma - \phi/2l; \theta, 0). \quad (29)$$

Next we analyze the FWM signal \mathcal{E}_2 for a similar path on the input sphere $\mathcal{O}(1, 0)$, going through points 1, 2, and 3 and ending at point 4, the negative pole, $(\theta, \phi) = (\pi, \pi/2)$. On this position, the incident mode is $\psi_{1,0}(\pi, \pi/2) = u_{-1,0}$. In Fig. 7(a) we show the paths followed by $u_a = \psi_{1,0}(\theta, \phi)$ (left), and by the generated field $\mathcal{E}_2 \propto \psi_{1,0}(\pi - \theta, \phi)$ (right). We divide the complete path 1–4 into three sections, and in Fig. 7(b) we illustrate how the incident and generated mode vectors change on the sphere in each section. In Fig. 7(c) we show the detected images of the intensity profiles of the incident field u_a at each position (top) and the resulting FWM signal \mathcal{E}_2 in each case (bottom). For points 1 and 4 the insets show the tilted lens (TL) profiles, indicating that in these positions the input and FWM fields possess opposite OAM. Along the arc 2–3 the input and generated field modes are degenerate in the sense that the position vector on the first-order sphere is the same. These results indicate the fulfillment of the reflection symmetry for signal \mathcal{E}_2 .

V. CONCLUSIONS

In this work, we have investigated the transfer of spatial structures from the input pump fields to the converted fields in a FWM degenerated process in a Rb vapor cell. We have

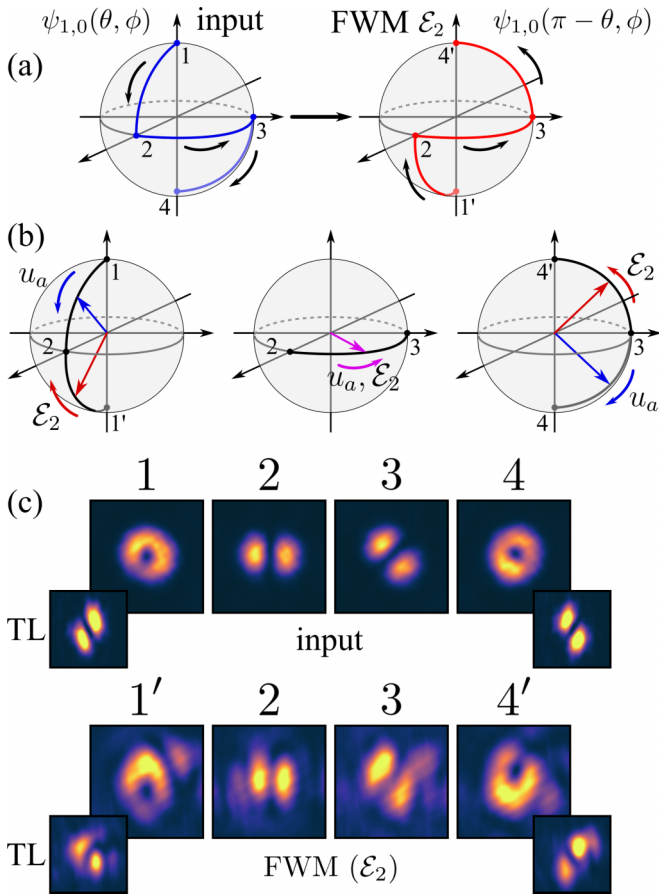


FIG. 7. (a) Path followed by the input mode $u_a = \psi_{1,0}(\theta, \phi)$ passing through points 1, 2, 3, and 4 on the sphere $\mathcal{O}(1, 0)$, and the corresponding path followed by the FWM signal $\mathcal{E}_2 \propto \psi_{1,0}(\pi - \theta, \phi)$, going through points 1', 2, 3, and 4'. The path on the generated field sphere is a reflection of the path on the input sphere with respect to the equatorial plane. (b) Sections 1, 1'-2, 2-3, and 3-4, 4' and the variation of the mode vectors of u_a and \mathcal{E}_2 in each one. (c) Detected far-field intensity profiles of the input and FWM signals at the points 1, 1', 2, 3, and 4, 4'. For points 1, 1' and 4, 4' we also show in the insets the tilted lens (TL) profiles, indicating opposite OAM between input and FWM fields.

analyzed that the whole interaction can be seen as a two-channel three-wave mixing process, whose spatial structures for the converted fields are independently driven by the square of one input field times the conjugate of the other field. By setting one of the input fields in a fundamental Gaussian mode, we have shown that the spatial structure of each conversion channel, in a thin medium, will be equivalent to what takes place in a second-order harmonic generation (SHG) and in a parametric down-conversion (PDC) for the fields \mathcal{E}_1 and \mathcal{E}_2 , respectively.

This allowed us to simultaneously explore the symmetries previously reported for these nonlinear processes [38,39], by structuring the other input field in an OAM Poincaré sphere $\mathcal{O}(l, 0)$. In particular, it was possible to observe the specular reflection symmetry for the field \mathcal{E}_2 with respect to the equatorial plane in the OAM sphere. We have also shown that the spatial structure of the other channel (\mathcal{E}_1) is a combination of two effects: the generation of radial order modes, and an

inner symmetry for the OAM components, similar to what was predicted for a three-wave mixing process [39]. This simultaneous two-channel symmetry of spatial modes can be useful for parallel generation and transmission of correlated fields for quantum information, as, for instance, the generation of multipartite entanglement within the spatial modes of the converted fields when the pump mode is in a superposition of high-order modes [54,55], where it has been shown that the entanglement structure can be tailored through the pump spatial mode [56,57]. In addition, OAM-multiplexed continuous-variable entanglement has been demonstrated in four-wave mixing, with important applications to quantum teleportation and quantum dense coding [33-36]. These applications can benefit from the symmetries reported here, since the OAM beams generated in the process are subjected to them and also to radial-angular coupling.

ACKNOWLEDGMENTS

This work was supported by CAPES (PROEX 534/2018, No. 23038.003382/2018-39); Instituto Nacional de Ciência e Tecnologia de Informação Quântica (INCT-IQ 465469/2014-0); Fundação de Amparo à Pesquisa do Estado de São Paulo (Grants No. 2021/06535-0 and No. 2021/06823-5). The authors would like to acknowledge the financial support from the Brazilian agencies: Conselho Nacional de Desenvolvimento Científico e Tecnológico (CNPq), Coordenação de Aperfeiçoamento de Pessoal de Nível Superior (CAPES), Fundação de Amparo à Ciência e Tecnologia de Pernambuco (FACEPE), Fundação Carlos Chagas Filho de Amparo à Pesquisa do Estado do Rio de Janeiro (FAPERJ). M.R.L.d.M. acknowledges financial support from CAPES (Grant No. 88887.623521/2021-00).

APPENDIX A: RADIAL MODE RESTRICTION ON THE REDUCED WAIST BASIS

As mentioned in the main text, with the appropriate choice of a beam waist, it is possible to restrict the number of radial orders contained in the output mode superpositions. In this Appendix we outline the calculation of the overlap integrals on the reduced beam waist basis, and make this restriction explicit.

The transverse overlap integral on the $\tilde{w} = w/\xi$ mode basis is

$$\tilde{\Lambda}_{q'np}^{ll'm\ell}(\xi) = \iint u_{l,q} u_{l',q'} u_{m,n}^* \tilde{u}_{\ell,p}^* |_{z=0} d^2 \mathbf{r}_\perp. \quad (\text{A1})$$

We now look at three different cases, corresponding to the coefficients \tilde{a}_0 , \tilde{b}_0 and \tilde{c}_p in Eqs. (22) and (23).

Let us focus first on the case $q = q' = m = n = 0$. The relevant integral is

$$\begin{aligned} \tilde{\Lambda}_{000p}^{ll'0\ell}(\xi) &= \iint u_{l,0} u_{l',0} u_{0,0}^* \tilde{u}_{\ell,p}^* |_{z=0} d^2 \mathbf{r}_\perp \\ &= 2\pi \delta_{\ell, l+l'} C_{l,0} C_{l',0} C_{0,0} C_{\ell,p} \xi^{|\ell|+1} \frac{1}{w^4} \\ &\times \int_0^\infty (r_w)^{|l|+|l'|+|\ell|} L_p^{|\ell|}(\xi^2 r_w^2) e^{-r_w^2(3+\xi^2)/2} r dr, \end{aligned} \quad (\text{A2})$$

where $r_w = \sqrt{2}r/w$. The choice $\xi = \sqrt{3}$ will be most interesting for us because it allows to establish a maximum value for the possibly coupled p orders. The only nonzero coefficients are those with $\ell = l + l'$,

$$\begin{aligned} \tilde{\Lambda}_{000p}^{l'l'+l'}(\sqrt{3}) &= \frac{8}{\pi w^4} \sqrt{\frac{p! 3^{-|l|-|l'|}}{|l|! |l'|! (p+|l+l'|)!}} \\ &\times \int_0^\infty (3r_w^2)^{|l+l'|} (3r_w^2)^p L_p^{|l+l'|} (3r_w^2) e^{-3r_w^2} r dr, \end{aligned} \quad (\text{A3})$$

where $P = (|l| + |l'| - |l + l'|)/2$. Then

$$\begin{aligned} \tilde{\Lambda}_{000p}^{l'l'+l'}(\sqrt{3}) &= \frac{4}{\pi w^2} \sqrt{\frac{p! 3^{-1-|l|-|l'|}}{|l|! |l'|! (p+|l+l'|)!}} \\ &\times \int_0^\infty x^{|l+l'|} x^p L_p^{|l+l'|}(x) e^{-x} dx. \end{aligned} \quad (\text{A4})$$

1. Coefficients \tilde{a}_0 for the sphere modes contained in \mathcal{E}_1

For $l \cdot l' \geq 0$, $P = 0$, and we can substitute x^p by $L_0^{|l+l'|}(x) = 1$. Using the orthogonality relation of the associated Laguerre polynomials, $\int_0^\infty x^\alpha L_p^\alpha(x) L_q^\alpha(x) e^{-x} dx = \frac{\Gamma(p+\alpha+1)}{p!} \delta_{p,q}$, we can write

$$\tilde{\Lambda}_{000p}^{l'l'+l'}(\sqrt{3}) = \begin{cases} \frac{4}{\sqrt{3}\pi w^2} \sqrt{\frac{|l+l'|!}{|l|! |l'|! 3^{|l+l'|}}} & \text{for } p = 0 \\ 0 & \text{for } p > 0. \end{cases} \quad (\text{A5})$$

We then see that no radial order $p > 0$ is generated.

2. Coefficients \tilde{c}_p for the radial modes contained in \mathcal{E}_1

Now, for $l \cdot l' < 0$, $P = \min(|l|, |l'|)$, and we expand the monomial x^p in terms of Laguerre polynomials as $x^n = n! \sum_{j=0}^n (-1)^j \binom{n+\alpha}{n-j} L_j^\alpha(x) = n! \sum_{j=0}^n b_{j,n}^\alpha L_j^\alpha(x)$, with $\alpha = |l + l'|$, to write

$$\begin{aligned} \tilde{\Lambda}_{000p}^{l'l'+l'}(\sqrt{3}) &= \frac{4}{\pi w^2} \sqrt{\frac{p! 3^{-1-|l|-|l'|}}{|l|! |l'|! (p+|l+l'|)!}} P! \sum_{j=0}^P b_{j,P}^{l+l'} \\ &\times \int_0^\infty x^{|l+l'|} L_j^{|l+l'|}(x) L_p^{|l+l'|}(x) e^{-x} dx. \end{aligned} \quad (\text{A6})$$

The x integral is once again the orthogonality relation of the associated Laguerre polynomials. Finally, we obtain

$$\begin{aligned} \tilde{\Lambda}_{000p}^{l'l'+l'}(\sqrt{3}) &= \frac{4}{\pi w^2} \frac{(-1)^p}{(P-p)!} \sqrt{\frac{3^{-1-|l|-|l'|}}{|l|! |l'|! p!(p+|l+l'|)!}} \\ &\times P!(P+|l+l'|)!, \end{aligned} \quad (\text{A7})$$

for $p \leq P$, and $\tilde{\Lambda}_{000p}^{l'l'+l'}(\sqrt{3}) = 0$, for $p > P$. This result is simplified in the case $l' = -l$, which makes $P = |l|$, and we get

$$\tilde{\Lambda}_{000p}^{l,-l}(\sqrt{3}) = \begin{cases} \frac{4}{\sqrt{3}\pi w^2} \frac{(-1)^p}{(|l|-p)!} \frac{|l|!}{p! 3^{|l|}} & \text{for } p \leq |l| \\ 0 & \text{for } p > |l|. \end{cases} \quad (\text{A8})$$

3. Coefficients \tilde{b}_0 for the sphere modes contained in \mathcal{E}_2

Next, for $l = l' = q = q' = n = 0$, we have

$$\begin{aligned} \tilde{\Lambda}_{000p}^{00m\ell}(\xi) &= \iint u_{0,0}^2 u_{m,0}^* \tilde{u}_{\ell,p}^* d^2 \mathbf{r}_\perp \\ &= 2\pi \delta_{\ell,-m} C_{0,0}^2 C_{m,0} C_{\ell,0} \xi^{|\ell|+1} \frac{1}{w^4} \\ &\times \int_0^\infty (r_w)^{|m|+|\ell|} L_p^{|\ell|}(\xi^2 r_w^2) e^{-r_w^2(3+\xi^2)/2} r dr. \end{aligned} \quad (\text{A9})$$

The OAM conservation dictates $\ell = -m$, and thus for $\xi = \sqrt{3}$ we can arrive at the expression

$$\tilde{\Lambda}_{000p}^{00m,-m}(\sqrt{3}) = \frac{4}{\pi w^2} \sqrt{3^{-1-|m|}} \frac{(2|m|)!}{(|m|!)^2} \delta_{p,0}. \quad (\text{A10})$$

APPENDIX B: COEFFICIENTS FOR CHANGING WAIST BASES

We may expand the mode $u_{\ell,p}$, with waist w , on the basis of modes $\tilde{u}_{l,q}$, with waist $\tilde{w} = w/\xi$, as

$$u_{\ell,p} = \sum_{l,q} \lambda_{p,q}^{\ell,l}(\xi) \tilde{u}_{l,q}, \quad (\text{B1})$$

where the expansion coefficients are

$$\lambda_{p,q}^{\ell,l}(\xi) = \iint u_{\ell,p} \tilde{u}_{l,q}^* |_{z=0} d^2 \mathbf{r}_\perp. \quad (\text{B2})$$

Since we must have $\ell = l$, we drop one of the upper indices, to write

$$\begin{aligned} \lambda_{p,q}^\ell(\xi) &= \frac{\pi}{2} C_{\ell,p} C_{\ell,q} \xi^{|\ell|+1} \\ &\times \int_0^\infty x^{|\ell|} L_p^{|\ell|}(x) L_q^{|\ell|}(\xi^2 x) e^{-x(1+\xi^2)/2} dx, \end{aligned} \quad (\text{B3})$$

where we made the change of variable $x = 2r^2/w^2$. For $\xi = 1$, we obtain $\lambda_{p,q}^\ell(1) = \delta_{p,q}$, which is expected. To obtain an analytical expression, we can employ the generating function for the Laguerre polynomials $\sum_{n=0}^\infty t^n L_n^\alpha(x) = (1-t)^{-(\alpha+1)} e^{-tx/(1-t)}$. Differentiating p times with respect to t , and making $t = 0$, we get

$$L_p^\alpha(x) = \frac{1}{p!} \frac{\partial^p}{\partial t^p} \left[\frac{e^{-tx/(1-t)}}{(1-t)^{\alpha+1}} \right] \Big|_{t=0}, \quad (\text{B4})$$

and we can rewrite the integral in Eq. (B3) as

$$\begin{aligned} &\frac{1}{p!q!} \frac{\partial^p}{\partial t^p} \frac{\partial^q}{\partial t'^q} \frac{1}{[(1-t)(1-t')]^{|\ell|+1}} \int_0^\infty x^{|\ell|} e^{-b(t,t')x} dx \\ &= \frac{|\ell|!}{p!q!} \frac{\partial^p}{\partial t^p} \frac{\partial^q}{\partial t'^q} \frac{1}{[b(t,t')(1-t)(1-t')]^{|\ell|+1}} \Big|_{t,t'=0}, \end{aligned} \quad (\text{B5})$$

with $b(t,t') = \frac{1+\xi^2}{2} + t/(1-t) + \xi^2 t'/(1-t')$. By carrying the indicated calculations, one obtains

$$\begin{aligned} \lambda_{p,q}^\ell(\xi) &= (-1)^p \sqrt{\frac{p!q!}{(|\ell|+p)! (|\ell|+q)!}} \left(\frac{2\xi}{1+\xi^2} \right)^{|\ell|+1} \\ &\times \sum_{n=0}^p (-1)^n \frac{(q+p+|\ell|-n)!}{n!(p-n)!(q-n)!} \left(\frac{1-\xi^2}{1+\xi^2} \right)^{q+p-2n}. \end{aligned} \quad (\text{B6})$$

- [1] H. Rubinsztein-Dunlop, A. Forbes, M. V. Berry, M. R. Dennis, D. L. Andrews, M. Mansuripur, C. Denz, C. Alpmann, P. Banzer, T. Bauer *et al.*, Roadmap on structured light, *J. Opt.* **19**, 013001 (2017).
- [2] A. Forbes, M. de Oliveira, and M. R. Dennis, Structured light, *Nat. Photonics* **15**, 253 (2021).
- [3] G. F. Calvo, A. Picón, and E. Bagan, Quantum field theory of photons with orbital angular momentum, *Phys. Rev. A* **73**, 013805 (2006).
- [4] K. E. Ballantine, J. F. Donegan, and P. R. Eastham, There are many ways to spin a photon: Half-quantization of a total optical angular momentum, *Sci. Adv.* **2**, e1501748 (2016).
- [5] C. Cai, L. Ma, J. Li, H. Guo, K. Liu, H. Sun, and J. Gao, Experimental characterization of continuous-variable orbital angular momentum entanglement using Stokes-operator basis, *Opt. Express* **26**, 5724 (2018).
- [6] I. Nape, B. Sephton, P. Ornelas, C. Moodley, and A. Forbes, Quantum structured light in high dimensions, *APL Photonics* **8**, 051101 (2023).
- [7] S. Franke-Arnold, J. Leach, M. J. Padgett, V. E. Lembessis, D. Ellinas, A. J. Wright, J. M. Girkin, P. Öhberg, and A. S. Arnold, Optical ferris wheel for ultracold atoms, *Opt. Express* **15**, 8619 (2007).
- [8] B. Melo, I. Brandão, B. P. da Silva, R. B. Rodrigues, A. Z. Khoury, and T. Guerreiro, Optical trapping in a dark focus, *Phys. Rev. Appl.* **14**, 034069 (2020).
- [9] A. C. Mandal, T. Sarkar, Z. Zalevsky, and R. K. Singh, Structured transmittance illumination coherence holography, *Sci. Rep.* **12**, 4564 (2022).
- [10] A. E. Willner, H. Huang, Y. Yan, Y. Ren, N. Ahmed, G. Xie, C. Bao, L. Li, Y. Cao, Z. Zhao, J. Wang, M. P. J. Lavery, M. Tur, S. Ramachandran, A. F. Molisch, N. Ashrafi, and S. Ashrafi, Optical communications using orbital angular momentum beams, *Adv. Opt. Photonics* **7**, 66 (2015).
- [11] L. Gong, Q. Zhao, H. Zhang, X.-Y. Hu, K. Huang, J.-M. Yang, and Y.-M. Li, Optical orbital-angular-momentum-multiplexed data transmission under high scattering, *Light Sci. Appl.* **8**, 27 (2019).
- [12] P. Gregg, P. Kristensen, A. Rubano, S. Golowich, L. Marrucci, and S. Ramachandran, Enhanced spin orbit interaction of light in highly confining optical fibers for mode division multiplexing, *Nat. Commun.* **10**, 4707 (2019).
- [13] Z.-Y. Zhou, Y. Li, D.-S. Ding, W. Zhang, S. Shi, and B.-S. Shi, Classical to quantum optical network link for orbital angular momentum-carrying light, *Opt. Express* **23**, 18435 (2015).
- [14] M. Al-Amri, D. Andrews, and M. Babiker, *Structured Light for Optical Communication* (Elsevier Science, Amsterdam, 2021).
- [15] F. Töppel, A. Aiello, C. Marquardt, E. Giacobino, and G. Leuchs, Classical entanglement in polarization metrology, *New J. Phys.* **16**, 073019 (2014).
- [16] T. Roger, J. J. F. Heitz, E. M. Wright, and D. Faccio, Non-collinear interaction of photons with orbital angular momentum, *Sci. Rep.* **3**, 3491 (2013).
- [17] S.-M. Li, L.-J. Kong, Z.-C. Ren, Y. Li, C. Tu, and H.-T. Wang, Managing orbital angular momentum in second-harmonic generation, *Phys. Rev. A* **88**, 035801 (2013).
- [18] L. J. Pereira, W. T. Buono, D. S. Tasca, K. Dechoum, and A. Z. Khoury, Orbital-angular-momentum mixing in type-II second-harmonic generation, *Phys. Rev. A* **96**, 053856 (2017).
- [19] X. Y. Z. Xiong, A. Al-Jarro, L. J. Jiang, N. C. Panoiu, and W. E. I. Sha, Mixing of spin and orbital angular momenta via second-harmonic generation in plasmonic and dielectric chiral nanostructures, *Phys. Rev. B* **95**, 165432 (2017).
- [20] W. T. Buono, J. Santiago, L. J. Pereira, D. S. Tasca, K. Dechoum, and A. Z. Khoury, Polarization-controlled orbital angular momentum switching in nonlinear wave mixing, *Opt. Lett.* **43**, 1439 (2018).
- [21] R. F. Offer, A. Daffurn, E. Riis, P. F. Griffin, A. S. Arnold, and S. Franke-Arnold, Gouy phase-matched angular and radial mode conversion in four-wave mixing, *Phys. Rev. A* **103**, L021502 (2021).
- [22] L. Allen, M. W. Beijersbergen, R. J. C. Spreeuw, and J. P. Woerdman, Orbital angular momentum of light and the transformation of Laguerre-Gaussian laser modes, *Phys. Rev. A* **45**, 8185 (1992).
- [23] K. Dholakia, N. B. Simpson, M. J. Padgett, and L. Allen, Second-harmonic generation and the orbital angular momentum of light, *Phys. Rev. A* **54**, R3742(R) (1996).
- [24] J. Courtial, K. Dholakia, L. Allen, and M. J. Padgett, Second-harmonic generation and the conservation of orbital angular momentum with high-order Laguerre-Gaussian modes, *Phys. Rev. A* **56**, 4193 (1997).
- [25] A. Beržanskis, A. Matijošius, A. Piskarskas, V. Smilgevičius, and A. Stabinis, Sum-frequency mixing of optical vortices in nonlinear crystals, *Opt. Commun.* **150**, 372 (1998).
- [26] V. Boyer, A. M. Marino, R. C. Pooser, and P. D. Lett, Entangled images from four-wave mixing, *Science* **321**, 544 (2008).
- [27] G. Walker, A. S. Arnold, and S. Franke-Arnold, Trans-spectral orbital angular momentum transfer via four-wave mixing in Rb vapor, *Phys. Rev. Lett.* **108**, 243601 (2012).
- [28] A. M. Akulshin, R. J. McLean, E. E. Mikhailov, and I. Novikova, Distinguishing nonlinear processes in atomic media via orbital angular momentum transfer, *Opt. Lett.* **40**, 1109 (2015).
- [29] A. M. Akulshin, I. Novikova, E. E. Mikhailov, S. A. Suslov, and R. J. McLean, Arithmetic with optical topological charges in stepwise-excited Rb vapor, *Opt. Lett.* **41**, 1146 (2016).
- [30] R. F. Offer, D. Stulga, E. Riis, S. Franke-Arnold, and A. S. Arnold, Spiral bandwidth of four-wave mixing in Rb vapour, *Commun. Phys.* **1**, 84 (2018).
- [31] A. Chopinaud, M. Jacquy, B. Viaris de Lesegno, and L. Pruvost, High helicity vortex conversion in a rubidium vapor, *Phys. Rev. A* **97**, 063806 (2018).
- [32] N. Prajapati, N. Super, N. R. Lanning, J. P. Dowling, and I. Novikova, Optical angular momentum manipulations in a four-wave mixing process, *Opt. Lett.* **44**, 739 (2019).
- [33] X. Pan, S. Yu, Y. Zhou, K. Zhang, K. Zhang, S. Lv, S. Li, W. Wang, and J. Jing, Orbital-angular-momentum multiplexed continuous-variable entanglement from four-wave mixing in hot atomic vapor, *Phys. Rev. Lett.* **123**, 070506 (2019).
- [34] S. Liu, Y. Lou, and J. Jing, Orbital angular momentum multiplexed deterministic all-optical quantum teleportation, *Nat. Commun.* **11**, 3875 (2020).
- [35] Y. Chen, S. Liu, Y. Lou, and J. Jing, Orbital angular momentum multiplexed quantum dense coding, *Phys. Rev. Lett.* **127**, 093601 (2021).
- [36] S. Li, X. Pan, Y. Ren, H. Liu, S. Yu, and J. Jing, Deterministic generation of orbital-angular-momentum multiplexed tripartite entanglement, *Phys. Rev. Lett.* **124**, 083605 (2020).

- [37] M. J. Padgett and J. Courtial, Poincaré-sphere equivalent for light beams containing orbital angular momentum, *Opt. Lett.* **24**, 430 (1999).
- [38] R. B. Rodrigues, J. Gonzales, B. P. da Silva, J. A. O. Huguenin, M. Martinelli, R. M. de Araújo, C. E. R. Souza, and A. Z. Khoury, Orbital angular momentum symmetry in a driven optical parametric oscillator, *Opt. Lett.* **43**, 2486 (2018).
- [39] R. B. Rodrigues, G. B. Alves, R. F. Barros, C. E. R. Souza, and A. Z. Khoury, Generalized orbital angular momentum symmetry in parametric amplification, *Phys. Rev. A* **105**, 013510 (2022).
- [40] B. P. da Silva, W. T. Buono, L. J. Pereira, D. S. Tasca, K. Dechoum, and A. Z. Khoury, Spin to orbital angular momentum transfer in frequency up-conversion, *Nanophotonics* **11**, 771 (2022).
- [41] W. T. Buono, L. F. C. Moraes, J. A. O. Huguenin, C. E. R. Souza, and A. Z. Khoury, Arbitrary orbital angular momentum addition in second harmonic generation, *New J. Phys.* **16**, 093041 (2014).
- [42] W. T. Buono, A. Santos, M. R. Maia, L. J. Pereira, D. S. Tasca, K. Dechoum, T. Ruchon, and A. Z. Khoury, Chiral relations and radial-angular coupling in nonlinear interactions of optical vortices, *Phys. Rev. A* **101**, 043821 (2020).
- [43] A. G. de Oliveira, G. Santos, N. R. da Silva, L. J. Pereira, G. B. Alves, A. Z. Khoury, and P. H. S. Ribeiro, Beyond conservation of orbital angular momentum in stimulated parametric down-conversion, *Phys. Rev. Appl.* **16**, 044019 (2021).
- [44] B. Coutinho dos Santos, C. E. R. Souza, K. Dechoum, and A. Z. Khoury, Phase conjugation and adiabatic mode conversion in a driven optical parametric oscillator with orbital angular momentum, *Phys. Rev. A* **76**, 053821 (2007).
- [45] B. Coutinho dos Santos, K. Dechoum, and A. Z. Khoury, Continuous-variable hyperentanglement in a parametric oscillator with orbital angular momentum, *Phys. Rev. Lett.* **103**, 230503 (2009).
- [46] K. Liu, J. Guo, C. Cai, S. Guo, and J. Gao, Experimental generation of continuous-variable hyperentanglement in an optical parametric oscillator, *Phys. Rev. Lett.* **113**, 170501 (2014).
- [47] P. H. Souto Ribeiro, D. P. Caetano, M. P. Almeida, J. A. Huguenin, B. Coutinho dos Santos, and A. Z. Khoury, Observation of image transfer and phase conjugation in stimulated down-conversion, *Phys. Rev. Lett.* **87**, 133602 (2001).
- [48] A. G. de Oliveira, M. F. Z. Arruda, W. C. Soares, S. P. Walborn, A. Z. Khoury, A. Kanaan, P. H. S. Ribeiro, and R. M. de Araújo, Phase conjugation and mode conversion in stimulated parametric down-conversion with orbital angular momentum: A geometrical interpretation, *Braz. J. Phys.* **49**, 10 (2019).
- [49] M. R. L. da Motta, A. A. C. de Almeida, and S. S. Vianna, Spatial distribution of two symmetric four-wave-mixing signals induced by Gaussian beams, *Phys. Rev. A* **106**, 053502 (2022).
- [50] M. R. L. da Motta, A. A. C. de Almeida, and S. S. Vianna, Combinations of orbital angular momentum in two degenerate four-wave mixing processes in Rb vapor, *J. Opt.* **25**, 095501 (2023).
- [51] R. N. Lanning, Z. Xiao, M. Zhang, I. Novikova, E. E. Mikhailov, and J. P. Dowling, Gaussian-beam-propagation theory for nonlinear optics involving an analytical treatment of orbital-angular-momentum transfer, *Phys. Rev. A* **96**, 013830 (2017).
- [52] M. G. de Oliveira, L. J. Pereira, A. S. Santos, K. Dechoum, A. Bramati, and A. Z. Khoury, Radial-angular coupling in self-phase-modulation with structured light, *Phys. Rev. A* **108**, 013503 (2023).
- [53] Z. Zhang, Y. Gao, X. Li, X. Wang, S. Zhao, Q. Liu, and C. Zhao, Second harmonic generation of laser beams in transverse mode locking states, *Adv. Photonics* **4**, 026002 (2022).
- [54] K. Liu, J. Guo, C. Cai, J. Zhang, and J. Gao, Direct generation of spatial quadripartite continuous variable entanglement in an optical parametric oscillator, *Opt. Lett.* **41**, 5178 (2016).
- [55] C. Cai, L. Ma, J. Li, H. Guo, K. Liu, H. Sun, R. Yang, and J. Gao, Generation of a continuous-variable quadripartite cluster state multiplexed in the spatial domain, *Photonics Res.* **6**, 479 (2018).
- [56] K. Zhang, W. Wang, S. Liu, X. Pan, J. Du, Y. Lou, S. Yu, S. Lv, N. Treps, C. Fabre, and J. Jing, Reconfigurable hexapartite entanglement by spatially multiplexed four-wave mixing processes, *Phys. Rev. Lett.* **124**, 090501 (2020).
- [57] R. F. Barros, G. B. Alves, O. Pfister, and A. Z. Khoury, Quantum-controlled cluster states, *Phys. Rev. A* **104**, 033713 (2021).